Citation for published item:

Giani, Stefano and Hakula, Harri (2022) 'Free Vibration of Perforated Cylindrical Shells of Revolution: Asymptotics and Effective Material Parameters.', Computer Methods in Applied Mechanics and Engineering, 403 (A). p. 115700.

Further information on publisher's website:

https://doi.org/10.1016/j.cma.2022.115700

Available online at www.sciencedirect.com
ScienceDirect

Comput. Methods Appl. Mech. Engrg. 403 (2023) 115700

Computer methods in applied mechanics and engineering

www.elsevier.com/locate/cma

Free vibration of perforated cylindrical shells of revolution: Asymptotics and effective material parameters

Stefano Giani[a], Harri Hakula[b],*

[a] Durham University, School of Engineering and Computing Sciences, South Road, Durham, DH1 3LE, United Kingdom
[b] Aalto University, Department of Mathematics and System Analysis, P.O. Box 11100, FI–00076 Aalto, Finland

Received 4 July 2022; received in revised form 1 October 2022; accepted 1 October 2022
Available online 29 October 2022

Abstract

Free vibration characteristics of thin perforated shells of revolution vary depending not only on the dimensionless thickness of the shell but also on the perforation structure. For any given configuration there exists a critical value of the dimensionless thickness below which homogenisation fails. The failure occurs when the modes do not have corresponding counterparts in the non-perforated reference shell. Within the admissible range of thicknesses the uniform effective material parameters are derived with a minimisation process. During the process every observed mode is matched with a corresponding reference one using a problem-specific characterisation. The performance of the derived effective material parameters and hence the minimisation process is demonstrated with an extensive set of numerical experiments. Limitations of the proposed approach are reflected in relation to idealised trommel screen configurations.

MSC: 65C20; 65N12; 65N25; 65N30

Keywords: Eigenproblems; Perforations; Homogenisation; Shells of revolution

---

1. Introduction

Thin structures remain one of the most challenging and fascinating classes of common engineering constructions. In this paper we study free vibration of thin perforated shells of revolution, their asymptotics as the thickness tends to zero, and opportunities for homogenisation of the material parameters. There are many important applications especially for perforated cylinders, in particular, rotary dryers and material separation screens are devices that are expensive to manufacture and are subject to large static, dynamic, and contact loads.

Perforations add geometric complexity and hence degrees of freedom to numerical solution methods such as the finite element method (FEM). The homogenisation process attempts to find so-called *effective material parameters* that account for the effects of the perforations so that the simulations can be run on non-perforated, that is, reference structures.

Although thin structures are three-dimensional, it is standard practice to reduce the computational costs even before perforations by deriving equivalent two-dimensional models where the thickness becomes a parameter. For

---

* Corresponding author.
E-mail addresses: stefano.giani@durham.ac.uk (S. Giani), Harri.Hakula@aalto.fi (H. Hakula).

https://doi.org/10.1016/j.cma.2022.115700
0045-7825/

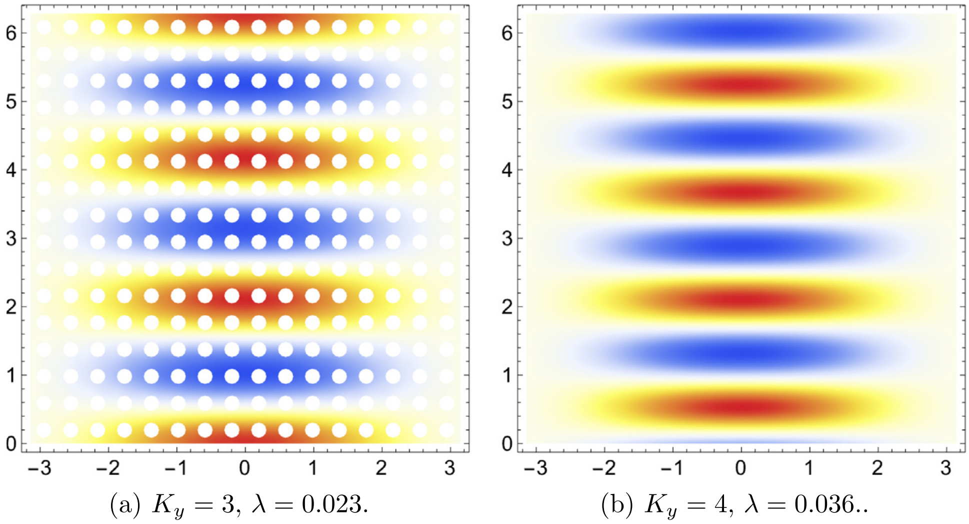

(a) $K_y = 3$, $\lambda = 0.023$.

(b) $K_y = 4$, $\lambda = 0.036$..

Fig. 1. (a) $t = 1/100$, 16×16-perforation grid with 25% hole coverage: Transverse deflection profile of the lowest mode. (b) $t = 1/100$, reference domain: Transverse deflection profile of the lowest mode.

analysis of the solutions it is advantageous to consider dimensionless thickness $t = d/L$, where d is the actual thickness and L is some characteristic length scale, for instance, the diameter of the domain. For our discussion we can use t and d interchangeably. In particular, shells have multiple boundary and internal layers, each with its own characteristic length scale. These local length scales can be expressed in terms of t, that is, they are parameter-dependent. Another important length scale is related to the perforation patterns, the cell size ϵ. Every perforated shell is assumed to have a fixed (constant) hole coverage percentage and a $g \times g$ -grid of circular holes, with $\epsilon \sim L/g$.

Straightforward approaches to homogenisation of material parameters, in other words, derivation of the effective material parameters, fail if the solutions have dominant local parameter-dependent features [1]. For modal analysis the interaction of the perforation pattern and the dimensionless thickness is the key. For shells of revolution the modes have integer valued wave numbers in the angular direction. When the characteristic length scales of the modes are smaller or equal than those of the perforation patterns, the modes will remain periodic, of course, but with non-trivial linear combinations of different wave numbers [2]. Given a perforation pattern, there exists a *critical thickness* t_c at which the structure of the modes changes and thus, a single homogenisation process cannot be valid over all thicknesses. This observation does not contradict the existing work on homogenisation but rather complements it — any asymptotic process simultaneously controlling both the perforation pattern and the thickness has to keep the latter above the corresponding critical value in order the maintain the inherent structure of the modes.

1.1. Novelty of this work

The eigenmodes of shells of revolution are parameter-dependent and the order in which they appear changes as the parameter changes. This is referred to as the mixing of modes. Therefore, one cannot assume that the first five modes, say, of the reference or non-perforated shell have the same characteristics as those of the perforated one, even if the dimensionless thickness is the same. In this context the homogenisation has to be considered in terms of subspaces rather than ordered parts of the spectrum. In Fig. 1 two examples, one perforated and another non-perforated, are shown. The angular wave number is different even though the shells have otherwise exactly the same characteristics.

The effective material parameters are derived through a minimisation process which relies on matching the observed modes on the perforated structures with the reference solutions. If this matching can be carried out, finding the effective material parameters reduces to a straightforward scaling problem. This means that the mode in Fig. 1(b) would not be directly affected by the mode of Fig. 1(a) unless the matching was between subspaces that happened to include them.

Interestingly, it is possible to detect exactly when the proposed scheme starts losing stability. At the critical thickness t_c two modes that belong to the same cluster in the reference problem may start drifting apart in the spectrum due to interaction of the perforation pattern and the dimensionless thickness. In other words, two modes with the same fingerprints have different eigenvalues. This *cluster separation* can exceed the initial spectral gap, that is, another cluster can exist in spectrum in between the modes of the original cluster. This phenomenon was observed in [2] but analysis of asymptotics presented here is new.

1.2. Brief review of literature

We refer to Martikka et al. [3] and Kalamkarov et al. [4] for many example applications for perforated cylinders. Terminology on perforations used in this paper is largely based on Forskitt [5] and Burgemeister [6].

Our original interest was piqued by a series of papers on an experimental nuclear reactor design [7–10]. Homogenisation of perforated structures has been studied by many authors both from theoretical and computational point-of-view. First, one can apply existing, general homogenisation methods to shell problems. Examples of this approach are, for instance, Kalamkarov et al. [4], which is an application of the multi-scale asymptotic homogenisation method [11], and Griso et al. [12], where homogenisation is derived by simultaneous homogenisation and dimension reduction within the framework of the periodic unfolding method [13]. Since thin shell models are dimensionally reduced from the corresponding elasticity ones, derivation of asymptotic limit models can be done in many different, yet mathematically rigorous, ways. Hornung et al. [14] start from the elasticity equations (possibly nonlinear) and derive homogenisation again by simultaneous homogenisation and dimension reduction.

There exists a substantial body of literature on related problems where the material used in the construction has some structure of its own, for instance, composites with varying properties in the thickness direction, see [15–17]. Similarly, various ribbed materials have been considered [18]. In a more abstract setting heterogeneity was considered by Sanchez-Palencia, see for instance [19]. Our discussion and numerical experiments are concerned with the dimensionally reduced models and therefore the results presented here are not directly applicable to materials with interesting properties in the thickness direction.

1.3. Structure of the discussion

First a high-level description of the proposed homogenisation workflow is given in Section 2. The shell eigenproblem is covered in detail in Section 3. The general geometry of shells of revolution is discussed, and the simplification leading to the mathematical shell model is motivated. The actual numerical methods are described in Section 4. Terminology and concepts related to perforations is briefly introduced in Section 5. The cluster structure of the shell eigenmodes and the associated parameter-dependent dynamics are discussed in Section 6. The all important mode identification is also discussed in that section. The minimisation process for finding the correct scaling, that is, homogenisation, is outlined in Section 7. Numerical examples and the case study of two trommel screens are followed by conclusions. In the appendix the Naghdi shell model is covered.

2. Homogenisation workflow

In this section a high-level description of the proposed homogenisation workflow is given. The central parameters defining the families of cylinders are a dimensionless thickness t, a diameter, i.e., radius R, and a perforation pattern and a hole coverage percentage, that together define a cell size ϵ. For the homogenisation process one has to account for the boundary conditions as well. The goal is to derive an effective material parameter, in this case Young's modulus, via an averaging scaling coefficient.

For vibration problems the homogenisation process should be applied on subspaces rather than simple modes. For symmetric structures, the modes have typically higher multiplicities (including the lowest modes), and any perturbations in the parameters may lead to mixing of the modes, where the modes belonging to the subspace change their relative positions within the spectrum.

For shells of revolution, the eigenmodes are periodic in the angular direction. This gives rise to simple characterisation of the modes in Fourier basis where every eigenpair is identified by an eigenvalue λ, and two wave numbers H and K, denoting axial and angular wave numbers, respectively. This is referred to as fingerprinting of the modes.

Assuming that the reference and perforated problems differ only in the perforation pattern and the hole coverage percentage, the overall process has the following stages, where the stages 1–3 can be computed offline:

- Stage 1: **Reference Database** A set of reference eigenproblems is solved and a database of mode fingerprints is created.
- Stage 2: **Perforated Problems** A set of eigenproblems with the given parametrisation is solved and another database of mode fingerprints is created.
- Stage 3: **Synthesis** For every mode in the database of perforated cases, the corresponding mode in the reference set is located and the averaged scaling factor based on the observed eigenvalues is computed.
- Stage 4: **Homogenised Solution** The eigenproblem is solved on non-perforated domain with the scaled material parameter.

In the sequel different stages are discussed in detail. In particular, the constraints of this approach are demonstrated via carefully designed experiments.

3. Shell eigenproblem

Assuming a time harmonic displacement field, the free vibration problem for a general shell leads to the following abstract *eigenvalue* problem: Find $\mathbf{u} \in \mathbb{R}^3$ and $\omega^2 \in \mathbb{R}$ such that

$$\begin{cases} \mathbf{S}\,\mathbf{u} = \omega^2 \mathbf{M}\,\mathbf{u} \\ + \text{ boundary conditions.} \end{cases} \tag{1}$$

Above, $\mathbf{u} = \{u, v, w\}$ represents the shell displacement field, while ω^2 represents the square of the eigenfrequency. In the abstract setting $\mathbf{S}$ and $\mathbf{M}$ are differential operators representing deformation energy and inertia, respectively. In the discrete setting they refer to corresponding stiffness and mass matrices.

In this paper two different dimensionally reduced shell models are considered: the mathematical shell model (shallow shell model) by Pitkäranta [20], and the classical Naghdi model [21]. For shells of revolution both models have natural one-dimensional variants after application of the same ansatz. The free vibration problem for a dimensionally reduced shell in the case of a shell of revolution with constant dimensionless thickness t leads to the following eigenvalue problem: Find $\mathbf{u}(t)$ and $\omega^2(t) \in \mathbb{R}$ such that

$$\begin{cases} t\,\mathbf{A}_M \mathbf{u}(t) + t\,\mathbf{A}_S \mathbf{u}(t) + t^3\,\mathbf{A}_B \mathbf{u}(t) = \omega^2(t)\,\mathbf{M}(t)\,\mathbf{u}(t) \\ + \text{ boundary conditions.} \end{cases} \tag{2}$$

Again, $\mathbf{u}(t)$ represents the shell displacement field, while $\omega^2(t)$ represents the square of the eigenfrequency. The differential operators $\mathbf{A}_M$, $\mathbf{A}_S$ and $\mathbf{A}_B$ defined above, account for membrane, shear, and bending potential energies, respectively, and are *independent of* t. Finally, $\mathbf{M}(t)$ is the inertia operator.

3.1. Parabolic shell of revolution

A cylinder is a parabolic shell with a constant radius, and is the simplest such structure. We start by introducing the connection between the exact shell geometry and the curvature tensor central to the mathematical shell model.

Thin shells of revolution can formally be characterised as domains in $\mathbb{R}^3$ of type

$$\Omega = \{\mathbf{x} + z\mathbf{n}(\mathbf{x}) \mid \mathbf{x} \in \omega, -d/2 < z < d/2\}, \tag{3}$$

where d is the (constant) thickness of the shell, ω is a (mid)surface of revolution, and $\mathbf{n}(\mathbf{x})$ is the unit normal to ω. For realistic geometries we assume principal curvature coordinates, where only four parameters, the radii of principal curvature R_1, R_2, and the so-called Lamé parameters, A_1, A_2, which relate coordinate changes to arc lengths, are needed to specify the curvature and the metric on ω.

The fundamental idea behind the dimension reduction is to transfer the problem onto a lower-dimensional computational domain with the constant thickness represented by a suitable parameter. We denote the computational

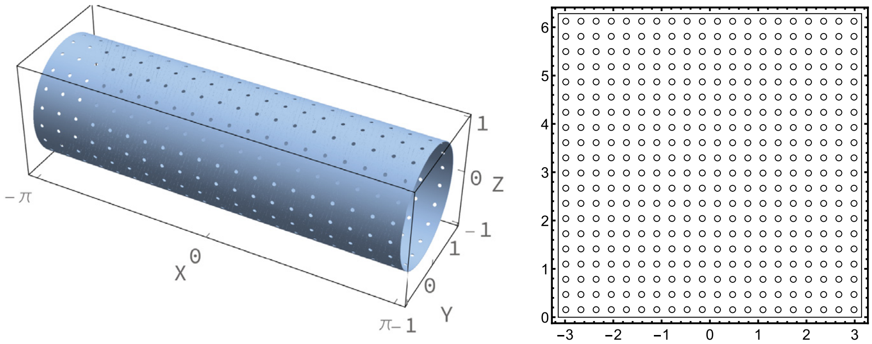

(a) $f_1(x_1) = 1,\ x_1 \in [-\pi, \pi]$.

(b) $D = [-\pi, \pi] \times [0, 2\pi]$

Fig. 2. Parabolic shell of revolution and the corresponding computational domain with a 20 × 20 regular perforation pattern with 12% hole coverage. For free vibration the boundaries at $x_1 = \pm\pi$ are clamped, holes are free, and $x_2 = 0$ and $x_2 = 2\pi$ are periodic.

domain with D (Fig. 2) and define it by unfolding ω as a rectangular domain expressed in the coordinates x_1 and x_2. This is the basis for the concepts of axial and angular directions below.

Furthermore, we assume that the curvature tensor $\{b_{ij}\}$ of the midsurface is constant, and as already mentioned in the introduction, in the sequel we replace the thickness d with the dimensionless thickness $t = d/L$, where $L \sim \mathrm{diam}(D)$.

Let us consider a cylindrical shell generated by a function $f_1(x_1) = 1$, $x_1 \in [-x_0, x_0]$, $x_0 > 0$. In this case the product of the Lamé parameters (metric), $A_1(x_1)A_2(x_1) = 1$, and the reciprocal curvature radii are $1/R_1(x_1) = 0$ and $1/R_2(x_1) = 1$, since

$$A_1(x_1) = \sqrt{1 + [f_1'(x_1)]^2}, \quad A_2(x_1) = f_1(x_1), \tag{4}$$

and

$$R_1(x_1) = -\frac{A_1(x_1)^3}{f''(x_1)}, \quad R_2(x_1) = A_1(x_1)A_2(x_1). \tag{5}$$

Thus, in the simplified model we can choose $b_{11} = 0$, $b_{22} = 1$, and $b_{12} = b_{21} = 0$, and arrive at a very good approximation of the exact geometry.

3.2. Mathematical shell model

Despite its simple form the mathematical shell model is one of the Reissner–Naghdi type shell models, where the transverse deflections are approximated with low-order polynomials. The Naghdi model is described in Appendix A. The resulting vector field has five components $\mathbf{u} = (u, v, w, \theta, \psi)$, where the first three are the displacements and the latter two are the rotations in the axial and angular directions, respectively. Here we adopt the convention that the computational domain D is given by the surface parametrisation and the axial/angular coordinates are denoted by x and y.

Deformation energy $\mathcal{F}(\mathbf{u})$ is divided into bending, membrane, and shear energies, denoted by b, m, and s, respectively.

$$\mathcal{F}(\mathbf{u}) = t^2 b(\mathbf{u}, \mathbf{u}) + m(\mathbf{u}, \mathbf{u}) + s(\mathbf{u}, \mathbf{u}). \tag{6}$$

Bending, membrane, and shear energies are given as

$$t^2\, b(\mathbf{u}, \mathbf{u}) = t^2 \int_D \Big[\nu(\kappa_{11}(\mathbf{u}) + \kappa_{22}(\mathbf{u}))^2 + (1-\nu)\sum_{i,j=1}^{2} \kappa_{ij}(\mathbf{u})^2\Big] dx\, dy, \tag{7}$$

$$m(\mathbf{u}, \mathbf{u}) = 12 \int_D \Big[\nu(\beta_{11}(\mathbf{u}) + \beta_{22}(\mathbf{u}))^2 + (1-\nu)\sum_{i,j=1}^{2} \beta_{ij}(\mathbf{u})^2\Big] dx\, dy, \tag{8}$$

$$s(\mathbf{u},\mathbf{u}) = 6(1-\nu)\int_D \Big[(\rho_1(\mathbf{u})^2 + \rho_2(\mathbf{u}))^2\Big] dx\,dy, \tag{9}$$

where ν is the Poisson ratio (constant). We have omitted the scaling $E/(12(1-\nu^2))$, where E is the Young's modulus. The strains are (with the curvature tensor values already inserted) as follows:

$$\begin{aligned}
\kappa_{11} &= \frac{\partial\theta}{\partial x}, \quad \kappa_{22} = \frac{\partial\psi}{\partial y}, \quad \kappa_{12} = \frac{1}{2}\left(\frac{\partial\theta}{\partial y} + \frac{\partial\psi}{\partial x}\right),\\
\beta_{11} &= \frac{\partial u}{\partial x}, \quad \beta_{22} = \frac{\partial v}{\partial y} + w, \quad \beta_{12} = \frac{1}{2}\left(\frac{\partial u}{\partial y} + \frac{\partial v}{\partial x}\right),\\
\rho_1 &= \frac{\partial w}{\partial x} - \theta, \quad \rho_2 = \frac{\partial w}{\partial y} - \psi.
\end{aligned} \tag{10}$$

Remarkably, these strains differ from those of the standard Naghdi model only in κ_{12} and ρ_1, when the radius is $= 1$. Naturally, for non-parabolic geometries the differences are much more extensive. Notice, that the resulting system has constant coefficients which simplifies the implementation of the model significantly.

3.3. Eigenmode ansatz

Due to the periodic structure every mode $\mathbf{u}(x,y)$ has either one of the forms

$$\mathbf{u}_1(x,y) = \begin{pmatrix} u(x)\cos(K\,y)\\ v(x)\sin(K\,y)\\ w(x)\cos(K\,y)\\ \theta(x)\cos(K\,y)\\ \psi(x)\sin(K\,y)\end{pmatrix} \text{ or } \mathbf{u}_2(x,y) = \begin{pmatrix} u(x)\sin(K\,y)\\ v(x)\cos(K\,y)\\ w(x)\sin(K\,y)\\ \theta(x)\sin(K\,y)\\ \psi(x)\cos(K\,y)\end{pmatrix}. \tag{11}$$

Remark 1. The two ansatz simply represent the trigonometric basis in the angular direction. Every eigenmode computed using a 1D model has a corresponding double eigenvalue in 2D with the exception of torsion modes.

For instance, using the first ansatz $\mathbf{u}_1(x,y)$, the strains have a form

$$\begin{aligned}
\kappa_{11} &= \frac{\partial\theta}{\partial x}, \quad \kappa_{22} = K\psi, \quad \kappa_{12} = \frac{1}{2}\left(-K\theta + \frac{\partial\psi}{\partial x}\right),\\
\beta_{11} &= \frac{\partial u}{\partial x}, \quad \beta_{22} = Kv + w, \quad \beta_{12} = \frac{1}{2}\left(-Ku + \frac{\partial v}{\partial x}\right),\\
\rho_1 &= \frac{\partial w}{\partial x} - \theta, \quad \rho_2 = -Kw - \psi.
\end{aligned} \tag{12}$$

Notice that the corresponding 1D energy definitions have the scaling π (2π, when $K = 0$). This 1D formulation allows us to compute extremely accurate reference solutions in the homogenisation process.

3.4. Variational formulation

Let us next consider the variational formulation of problem (2). The inertia operator in this case can be split into the sum $\mathbf{M}(t) = t\,M^l + t^3\,M^r$, with M^l (displacements) and M^r (rotations) *independent of* t. Accordingly, we introduce the space V of admissible displacements, and consider the problem: Find $(\mathbf{u}(t), \omega^2(t)) \in V \times \mathbb{R}$ such that

$$\begin{aligned}
t\,m(\mathbf{u}(t),\mathbf{v}(t)) + t\,s(\mathbf{u}(t),\mathbf{v}(t)) + t^3\,b(\mathbf{u}(t),\mathbf{v}(t)) &=\\
\omega^2(t)\,\mathbf{M}(t;\mathbf{u}(t),\mathbf{v}(t)) \quad \forall \mathbf{v} \in V&,
\end{aligned} \tag{13}$$

where $m(\cdot,\cdot)$, $s(\cdot,\cdot)$, $b(\cdot,\cdot)$ are the bilinear forms associated defined above.

Remark 2. The space V and the three bilinear forms depend on the chosen shell model (see for instance [21]).

In all cases the boundary conditions are the same: at the ends $x = \pm\pi$ the shell is clamped, that is, fully kinematically constrained, but all perforations are free.

4. Numerical method: *hp*-FEM

All numerical simulations reported here have been computed with two different high-order continuous Galerkin codes in 2D solving the variational formulation on conforming meshes of triangular elements. The first one is implemented with Mathematica, providing exact geometry handling of the holes via blending functions [22]. This code has been used to compute the examples with the Naghdi model and indirectly in calibration of the second solver.

The second one is a parallel code implemented in FORTRAN90 and MPI. The results reported on the mathematical shell model have been computed with this code. The code allows for a many different types of boundary conditions. Probably the most interesting one from the implementation point of view is the periodic boundary condition. This boundary condition is implemented identifying one-by-one the dof on opposite boundaries of the domain. It is assumed that identified boundaries are split in the same number of edges and that identified edges have same sizes. In general, Periodic boundary conditions reduce the global number of dof in the problem. This code allows for arbitrary order of polynomials to be used in the elements. The construction of the H^1-conforming triangular elements is based on [23], where the shape functions are defined hierarchically using Lobatto shapefunctions. Different order of polynomials can be used in different elements in the same mesh. To maximise flexibility, the code allows also for different order of polynomials on different components on the same element. Along the faces shared by adjacent elements with different order of polynomials, the higher order polynomial space on the face is projected onto the polynomial space on the face of the element of lower order. In this way, the number of dof along the face of the higher order element is reduced to match the number of dof on the same face of the element of lower order. Crucially, in order to minimise integration errors on complicated domains, the shape of the elements are represented using the transfinite interpolation method [23] which allows for the edges of the elements to be bent exactly to match the shape of the holes. Together with high order quadrature rules, the integration errors in the discrete problem are controlled. One such sample configuration is shown in Fig. 3.

The solution of the eigenvalue problems are computed using ARPACK [24] and MUMPS [25–27] as the linear solver called from inside ARPACK. To reduce the computational time and exploit parallelism of modern HPC machines, MPI is used in the assembly of the linear system and in MUMPS to approximate the eigenpairs. When MPI is used, the stiffness and mass matrices are split in consecutive chunks of rows. Each chunk is assigned to a processor. The matrices are assemble in parallel with the processors integrating over all elements with at least a dof assigned to them. This means that some elements are shared on more than one processor and so they are integrated independently on multiple processors avoiding any communication between processors during the matrix assembly. The eigenvalue problems are solved using the shift and invert method in ARPACK that allows to approximate the eigenpairs with eigenvalues close to a given value. To compute the bottom of the spectrum a value of zero is used.

Given this two-pronged simulation strategy, we have high confidence in the accuracy of the computed results and the conclusions drawn from them.

5. Perforated shells

Perforated domains are characterised by the penetration patterns which in turn depend on the underlying manufacturing processes and the related hole coverage, typically given as a percentage. Here we consider standard structured patterns only.

5.1. Regular penetration patterns

The quantity used to characterise perforated sheets of metal is the ligament efficiency η. Let us assume that the holes are ellipses with a, b as the horizontal and perpendicular semiaxis, and the separation of the centres is P_x and P_y, respectively. Following [5,8,28], we define horizontal and perpendicular ligament efficiency, denoting them η_x, η_y, respectively. For regular arrays of holes

$$\eta_x = (P_x - 2\,a)/P_x, \qquad \eta_y = (P_y - 2\,b)/P_y, \tag{14}$$

and for triangular arrays, allowing for alternating layers,

$$\eta_x = (P_x - 4\,a)/P_x, \qquad \eta_y = (P_y - 4\,b)/P_y. \tag{15}$$

For circular holes the radius $r = a = b$, of course, and further if the pattern is regular $\eta = \eta_x = \eta_y$.

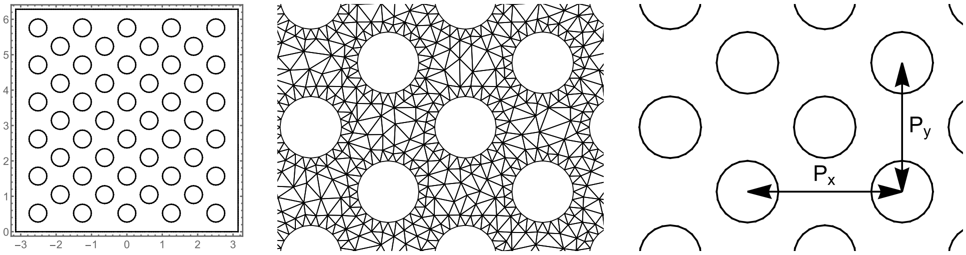

(a) Penetration pattern. (b) Mesh detail. (c) Ligament efficiency.

Fig. 3. Typical configuration: Hole coverage 25% (Radius of holes $r = 1/4$). In the detail, the hole is programmatically mapped to be circular in the assembly of the system and therefore much coarser meshes can be used. Here $P_x = 2\pi/5$ and $P_y = 2\pi/6$ and thus the ligament efficiencies are $\eta_x = 1 - 5/(2\pi) \approx 0.2$ and $\eta_y = 1 - 3/\pi \approx 0.05$. In the simulations the boundaries at $x_1 = \pm\pi$ are clamped, holes are free, and $x_2 = 0$ and $x_2 = 2\pi$ are periodic.

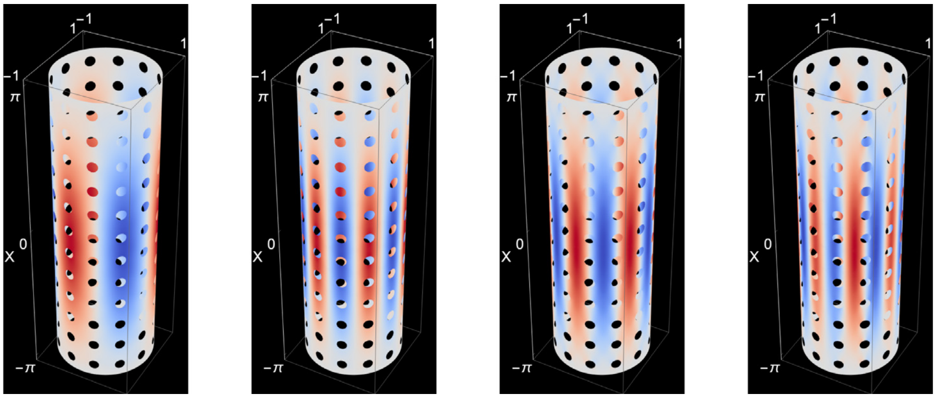

(a) $t \gg t_c$: Mode 1. (b) $t \approx t_c$: Mode 1. (c) $t \approx t_c$: Mode 4. (d) $t \ll t_c$: Mode 1.

Fig. 4. Examples of eigenmodes. Transverse deflection profiles of eigenmodes on 12×12 regular grid with hole coverage percentage of 12%. Illustration of the global and local feature ranges: (a), $t = 1/100 \gg t_c$, (b) and (c), $t = 0.007 \approx t_c$, and (d), $t = 0.0025 \ll t_c$. Notice the alignment with respect to the perforation pattern of the Modes 1 and 4 at $t \approx t_c$.

5.2. Internal layers and penetration patterns

The solution of a static shell problem can be viewed as a linear combination of features with characteristic length scales with the smooth component having the diameter of the whole shell. These features can be boundary layers but also internal layers.

For the eigenmodes in the parabolic reference case, the boundary layers do not carry significant amount of energy in the lower end of the spectrum. However, the angular wave numbers of the smallest eigenpairs are determined by the internal layers and their characteristic length scale, which is $L(t) \sim \sqrt[4]{t}$.

Let us consider a regular penetration pattern with some given ligament efficiency η and hence perpendicular separation P_y. Then there exists an integer valued angular wave number K_c for which the associated wave length is $\sim P_y/2$. For every mode with $K > K_c$ the effective loading by the mode becomes unevenly distributed over the holes and the solid parts. For these modes the angular oscillations cannot be characterised by a single wave number since the angular displacement profiles are periodic linear combinations of trigonometric functions.

In Figs. 4(b) and 4(c) examples of perfectly aligned modes are illustrated. In fact, the pair forms a natural cluster of eigenmodes. This will be elaborated in more detail in the next section.

Table 1
Known asymptotic eigenbehaviour of the smallest eigenpair of parabolic shells as $t \to 0$. Reference configuration $f(x_1) = 1$, i.e., $R = 1$.

Quantity of interest	Asymptotics
Eigenvalue	$\lambda(t) \sim t$
Angular wave number	$K(t) \sim t^{-1/4}$
Bending energy%	$B(t) \to 1/2$
Angular wave number with R	$K(t, R) \sim R^{3/4} t^{-1/4}$

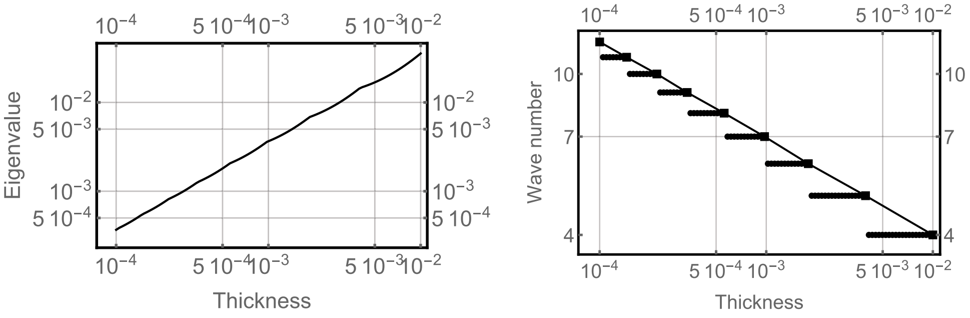

(a) $\lambda(t)$ (b) $K(t)$

Fig. 5. Reference asymptotic analysis: $R = 1$, $t \in [10^{-4}, 10^{-2}]$, uniform logarithmic scale with 100 samples. Expected rates: $\lambda(t) \sim t$; $K(t) \sim t^{-1/4}$.

6. Clusters and asymptotics: Constraints for homogenisation

One of the defining features of all shells of revolution is that the eigenmodes are clustered due to symmetries and the effect of the dimensionless thickness. For instance, all eigenvalues excluding the torsion ones have multiplicity of at least two. In contrast to second order problems, here also the smallest mode can have a higher algebraic order. In (11) the two ansatz were given, and in fact they can be thought of as the basis functions of the eigenspace in the angular direction.

In Table 1 the known asymptotics of the smallest eigenmode of cylindrical (parabolic) shells are listed. Since the angular wave numbers increase as $t \to 0$, it follows that for some thicknesses the multiplicity of the smallest eigenvalue is four.

For perforated shells of revolution the asymptotics of the smallest mode follow those of the reference case until a critical thickness t_c has been reached. At this point the cluster of size two is split and a gap between the eigenvalues emerges. There is a simple geometric explanation for this phenomenon: At the critical thickness t_c the wavelength of the smallest eigenmode is of the same order as the separation of the holes in the perforation pattern. It can even happen that some clusters with lower wave numbers (and therefore longer wavelengths) slide in between the modes of the original cluster. This is illustrated in Fig. 4. We refer to this phenomenon of the cluster breaking apart and thus the difference between the associated eigenvalues becoming nonzero as cluster separation.

The asymptotic reference eigenbehaviour for the cylinder with $R = 1$ is shown in Fig. 5. The non-standard convergence in bending energy as well as the dynamics of the modes are added in Fig. 6. For perforated cylinders the expected behaviour is the same for thicknesses greater than the critical t_c. In particular the energy ratios diverge from the reference as $t_c \gg t \to 0$, since the boundary layers around the holes start dominating locally and hence increase bending.

The dynamics of the modes (see Fig. 6(b)) mean that if the wavenumber of one of the higher modes is observed over a range of thicknesses, the resulting sequence is not necessarily monotone as in the case of the smallest mode. This is due to modes with higher wavenumbers entering the lower end of the spectrum and consequently ones with lower wavenumbers exiting that part of the spectrum.

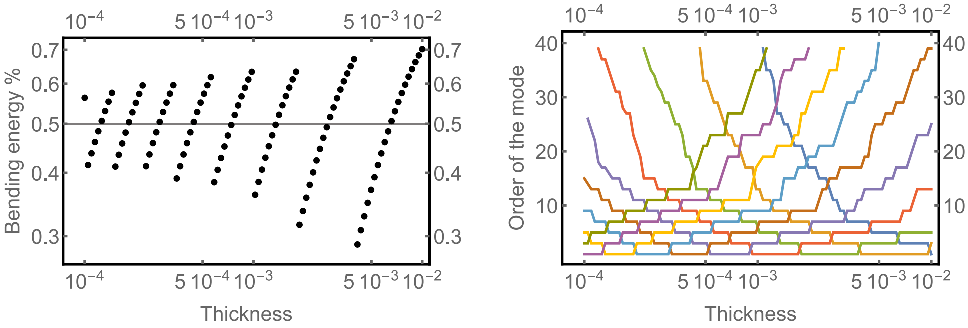

(a) Bending energy%: $B(t)$ (b) Relative ordering of modes

Fig. 6. Derived asymptotics: $R = 1$, $t \in [10^{-4}, 10^{-2}]$, uniform logarithmic scale with 100 samples. Expected rate: $B(t) \to 1/2$. (b) Different colours refer to different eigenmodes and their relative positions in the spectrum. The bottom line in each plot indicates the smallest mode the value of which can be inferred from the ranges of $K(t)$ in Fig. 5. The upper sections of the figure appear sparser, since only those modes that ever become the smallest ones are shown.

6.1. Identification of modes

For the proposed homogenisation scheme to work, it is necessary to be able to match eigenmodes, and as the discussion above indicates, this has to be based on the properties of the modes and not on the ordering of the spectrum.

In the case of free vibration we rely on the observation that at the lowest end of the spectrum the boundary layers are not the dominant features of the modes and hence, Fourier analysis is sufficient. For every mode both angular and axial wave numbers are computed, and together they form a mode key or fingerprint, for short.

For shells of revolution, the angular wave number is unambiguous, however, the axial one should include information on even/odd resolution — sine/cosine separation can be indicated with integer/rational indicators. For the two modes in Fig. 1 their respective fingerprints are (3, 1/2) and (4, 1/2). In the reference case there is always a unique eigenvalue in the eigenpair and of course, in the view of the two ansatz above, one fingerprint covers two modes with the same angular wave number. It is precisely at this point where cluster separation induces errors, symmetry will be broken.

7. Effective material parameters

Although the basic idea behind the derivation of the effective material parameters in the eigenproblem is the same as in the static case, there is one fundamental difference that adds another computational layer to the process. For the algorithm described in the following to be valid, one must be able to match the eigenpairs based on key characteristics of the modes rather than simple enumeration of the modes in the given case. Already in Fig. 1 an example of two smallest modes with non-matching key characteristic (angular wave number) was given.

7.1. Minimisation of single mode over representative cell

Let us next focus on how to find the multiplicative effective material parameter once the critical thickness has been established. Let $(\hat{\lambda}, \hat{u})$ be an eigenpair of the reference, that is, non-perforated, domain. The first goal is to find an eigenpair $(\lambda_0, u_0) \sim (\alpha\hat{\lambda}, \hat{u})$ to the non-perforated problem with a multiplicative constant α. Instead of operator formalism we use matrix notation and omit the dependence on the domain in matrices for now. Thus, in matrix notation the problem is

$$\alpha\, S u_0 = \lambda_0 M u_0,$$

where S and M are the stiffness and mass matrices, respectively. We proceed by choosing an admissible sequence of grids with ϵ_k, $k = 1, 2, \ldots, N$, and finding the eigenpairs to the perforated problems $(\lambda_{\epsilon_k}, u_{\epsilon_k})$, $k = 1, 2, \ldots, N$.

Formally, we seek the minimiser for the sum of the squares of errors in the L^2-norm,

$$\min_{(\lambda_0,u_0)\ \text{s.t.}\ \alpha\, Su_0=\lambda_0 Mu_0} \sum_k \|\lambda_0 u_0 - \lambda_{\epsilon_k} u_{\epsilon_k}\|_{L^2}^2.$$

If we assume that all modes are normalised in the L^2-norm, the minimisation reduces to simple averaging of the eigenvalues. Scalar scaling does not change the eigenmodes, so immediately $u_0 = \hat{u}$. First with

$$\sum_k \|(\alpha\hat{\lambda})u_0 - \lambda_{\epsilon_k} u_{\epsilon_k}\|_{L^2}^2 = \sum_k ((\alpha\hat{\lambda})u_0 - \lambda_{\epsilon_k} u_{\epsilon_k})^T M((\alpha\hat{\lambda})u_0 - \lambda_{\epsilon_k} u_{\epsilon_k}),$$

we get

$$= \sum_k (\alpha\hat{\lambda})^2 u_0^T\, M\, u_0 - 2\sum_k (\alpha\hat{\lambda})\lambda_{\epsilon_k} u_0^T\, M\, u_{\epsilon_k} + \text{const}.$$

Finally, under the normalisation assumption we compute the minimum for $\alpha\hat{\lambda}$. This is meaningful only if the modes match, since otherwise $u_0^T\, M\, u_{\epsilon_k} \neq 1$.

Putting everything together we have shown the following (formal) theorem

Theorem 3 (*Single Mode (Formal)*)**.** *Let the thickness $t \geq t_c$ be given. Let us denote the stiffness and standard mass matrices by S and M, respectively. Let $(\lambda_{\epsilon_k}, u_{\epsilon_k})$, $k = 1, 2, \ldots, N$, be a sequence of eigenpairs of perforated problems with every ϵ_k sufficiently small. Then the homogenised eigenpair (λ_0, u_0) is the minimiser of*

$$\min_{(\lambda_0,u_0)\ \text{s.t.}\ \alpha\, Ku_0=\lambda_0 Mu_0} \sum_k \|\lambda_0 u_0 - \lambda_{\epsilon_k} u_{\epsilon_k}\|_{L^2}^2.$$

and α is the effective multiplicative constant

$$\alpha = \frac{\sum_k \lambda_{\epsilon_k}}{N\lambda_0}.$$

We have carefully labelled the theorem as formal since in practice the computational domain Ω depends on ϵ and thus the derived matrices as well as already noted above. Theoretically it is clear that for the mass matrices $\mathcal{M}_\epsilon \to M$ as $\epsilon \to 0$, but for the stiffness ones similar convergence cannot hold.

7.2. Minimisation of subspace over representative cell

Extension of the minimisation procedure over a subspace is straightforward.

Corollary 1 (*Subspace (Formal)*)**.** *Let E_0 be the subspace spanned by the eigenmodes $\{u_0^1, \ldots, u_0^K\}$, on the reference (non-perforated) configuration, and $\Lambda_0 = \{\lambda_0^1, \ldots, \lambda_0^K\}$ the set of associated eigenvalues. Similarly, for every ϵ_k, $k = 1, 2, \ldots, N$, let E_{ϵ_k} and Λ_{ϵ_k} be the corresponding subspaces and sets. If α_j is the effective multiplicative constant for the eigenpair (λ_0^j, u_0^j), then their weighted average α is the effective multiplicative constant for the whole subspace:*

$$\alpha = \frac{\sum_j w_j \alpha_j}{\sum_j w_j},$$

where w_j are the weights.

8. Numerical experiments

The numerical experiments cover not only examples of the application of the homogenisation process but also the construction of the reference database which in the special case of shells of revolution can be done with further dimension reduction in 1D. For an overview of the experiments and details of discretisations, see Tables 2 and 3.

Table 2
Overview of the experiments.

Category	Options
Geometry	Parabolic
Penetration pattern	Regular
Grid size	20, 30, 40
Hole coverage	7%, 12%, 25%
Thickness	Logarithmic division, 100 samples, $t \in [10^{-4}, 10^{-2}]$
Subspace	12 modes

Table 3
Data on discretisations. Meshes used in simulations and the number of degrees of freedom at uniform $p = 5$. Since both shell models considered here use the same domain parametrisation, the same mesh has been used for both. Furthermore, the 2D discretisation does not depend on the radius of the shell of revolution.

%	g	Nodes	Edges	Triangles	DOF
7	20	11104	30509	19006	1235880
	30	16701	46600	29000	1885505
	40	29165	81892	51128	3317505
12	20	13357	35868	22112	1447505
	30	23700	65997	41398	2680380
	40	41800	41800	116797	4746880
25	20	8681	22040	12960	873005
	30	11080	28337	16358	1112880
	40	19440	49917	28878	1961880

8.1. Database construction

The process for setting up a database for reference solutions is the same for both shell models considered here. For every t considered, the 1D reference subspace (the first four modes) was computed for all angular integer wave numbers $K_y \in [0, K_{\max}]$. Here a priori knowledge existed for setting $K_{\max} = 20$. Further, for every reference solution an axial wave number H_x was derived using simple Fourier analysis. Finally, the process was repeated for every R used in Naghdi experiments.

Formally, the database construction leads to a map from the mode fingerprint in the non-perforated case to the corresponding eigenvalue. In the special case of shells of revolution, a sufficient identifier for every mode is a tuple: thickness, radius, and the two wave numbers, that is, for every unique mode m a map

$$\{t, R, K_y, H_x\}_m \to \{\lambda\}_m$$

exists.

Although the specific construction described here depends on the special structure of the reference case, in the general case such a reference should nevertheless always be identifiable and hence fingerprinting with a suitable mode key be possible. For instance, in our current setting there is no need to include boundary layer information in the mode key.

Remark 4. Notice that H_x should also include information on symmetry/antisymmetry of the mode. In the angular direction this is not necessary due to symmetry.

8.2. Perforated cases

The goal is to understand the performance of the minimisation process discussed in Section 7 over a sequence of dimensionless thicknesses. The dimension of the subspace (= 12) is arbitrary, however, it is even and sufficiently large to allow for perforation-dependent behaviour within the parameter range $t \in [10^{-4}, 10^{-2}]$. Typically in engineering literature the "practical" range is taken to be $t \in [10^{-3}, 10^{-2}]$. It is known that the grid size (or

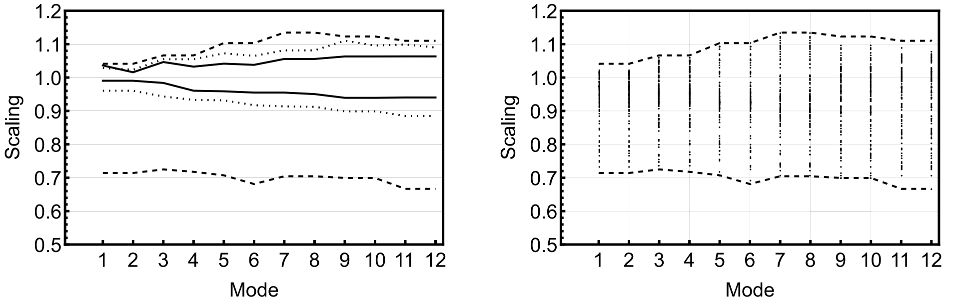

(a) Coverage dependent bounds over the modes.

(b) Spread of eigenvalues at 25% hole coverage over the modes.

Fig. 7. Homogenised eigenvalues. Ratios of homogenised eigenvalues over the observed ones. Perfect homogenisation would result in constant line = 1. Solid line: 7%, dotted: 12%, dashed: 25%.

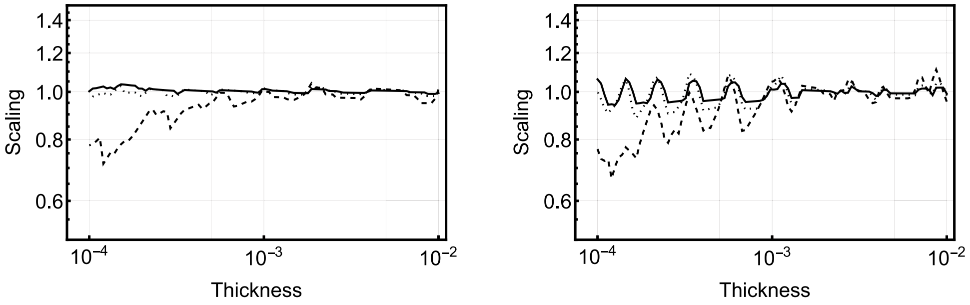

(a) Mode 1.

(b) Mode 12.

Fig. 8. Homogenised eigenvalues. Ratios of homogenised eigenvalues over the observed ones for the first and 12th modes. Perfect homogenisation would result in constant line = 1. Solid line: 7%, dotted: 12%, dashed: 25%.

equivalently, cell size) and the hole coverage are key parameters as well. The discussion here relies on averaged quantities of interest, which is appropriate in homogenisation context. More specifically, the accuracy of the homogenised eigenvalues is measured with their ratio over the observed ones, where value one would indicate perfect homogenisation.

In Fig. 7 the effect of the hole coverage is illustrated. As one would expect, the homogenised eigenvalues converge as the hole coverage decreases. The convergence is not uniform, with the higher modes showing slightly higher relative errors. In Fig. 7(b) the spread of relative values per mode with a fixed hole coverage percentage of 25% is shown. Overall, the interval is covered reasonably uniformly for every mode.

The dependence on the dimensionless thickness is the focus in Fig. 8. At 25% the relative performance deviates from that of both 12% and 7%. By close inspection of both Figs. 9 and 10 one can see that this occurs exactly in the range where the critical mode $K = 10$ enters subspace at grid $g = 20$. The loss of one-to-one correspondence between the perforated and reference modes pollutes the minimisation.

The coupling between the modes and the perforation pattern is independent of the hole coverage. In Fig. 9(b) the bar indicating the mode $K = 10$ is dramatically wider than those for $g = 30$ or $g = 40$. The mode dynamics are evident in Fig. 10. The wavenumber for the higher modes do not grow monotonically as explained above. This underlines the need for effective fingerprinting on the modes, since one cannot rely on any repeated patterns or rules beyond the smallest mode.

8.3. *Effect of radius*

Since the mathematical shell model does not have an explicit concept of the radius of the shell, it is necessary for us to use Naghdi model for the analysis of the effects of the radius and the diameter, of course, on the critical

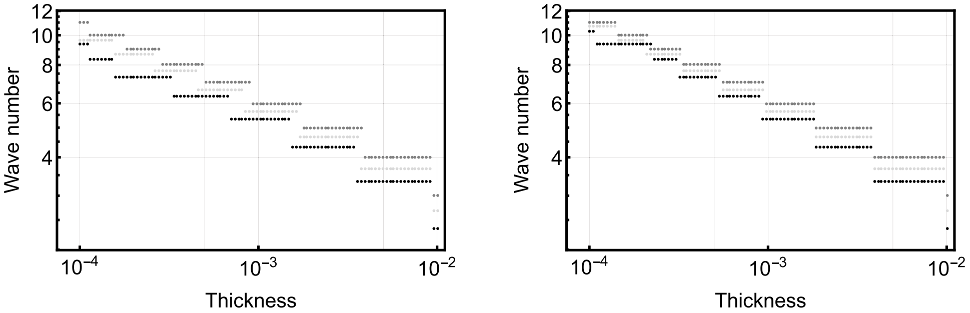

(a) Hole coverage 25%. (b) Hole coverage 7%.

Fig. 9. Homogenised eigenvalues. The lowest mode. The effect of hole coverage percentage on the wavenumber. Grid size $g =$, black: 20, light grey: 30, dark grey: 40. All values are integers, the black and light grey ones have been shifted by 2/3 and 1/3, respectively.

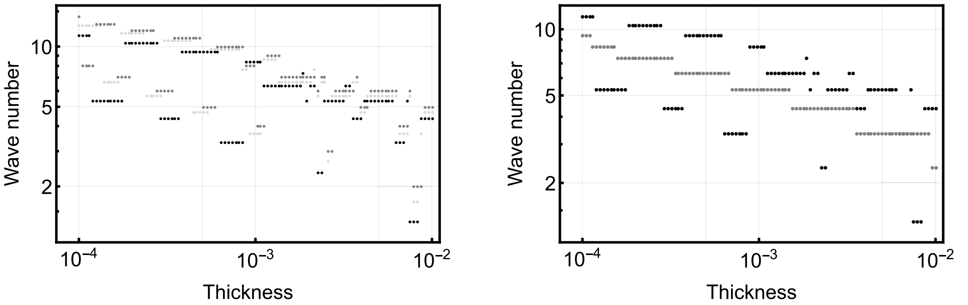

(a) Hole coverage 25%. (b) Hole coverage 25%: $g = 20$, modes 1 and 12.

Fig. 10. Homogenised eigenvalues. The mode 12. (a) The wavenumber asymptotics at 25%. Grid size $g =$, black: 20, light grey: 30, dark grey: 40. All values are integers, the black and light grey ones have been shifted by 2/3 and 1/3, respectively. (b) Comparison of the wavenumber asymptotics of the modes 1 and 12. Black: mode 12, dark grey: mode 1.

thickness. As above, the parameters remain the same: the dimensionless thickness t, the grid size g, and the angular wave number K.

Based on the results already presented above, it is no surprise that the same effects occur earlier in the thickness range (measured from above) as the radius increases, since the theory predicts that the critical thickness depends on the coupling between the modes and the perforation pattern, and indeed, the wave number increases as a function of the radius.

Both Figs. 11 and 12 indicate the strong coupling between $K = 10$ and $g = 20$. Especially the comparison of the bending energies in Fig. 12 reveals an almost dramatic difference in performance. Yet, the detail in Fig. 12(b) suggests that the same effect occurs also for $g = 30$ as $t \to 0$ or as $K \to 15$.

8.4. Asymptotics and cluster separation

Our final section within the experiments concerns the cluster separation. Using our a priori knowledge of the critical thickness, we can select the grid size and the associated wave number optimally. In Figs. 13 and 14 the selection is $g = 20$ and naturally $K = 10$. It is clear that every cluster (in the reference case) with $K = 10$ will have some separation in the perforated case with $g = 20$. Both the relative difference and the width or distance within the spectrum (mode number) is shown.

In all cases the separation width is an odd number. If the width is greater than one, then the natural interpretation is that a cluster (or clusters) of size two has moved within the original one. Indeed in Fig. 14 the width 11 shows that five clusters are within the original one.

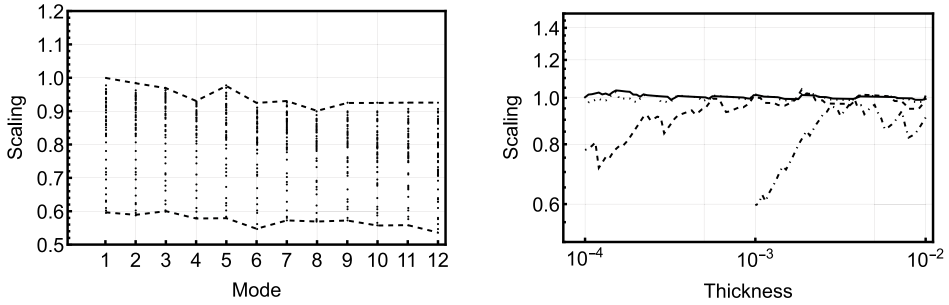

(a) Spread of eigenvalues at 25% hole coverage over the modes.

(b) Hole coverage 25%: The lowest mode $R = 1$ results augmented by those of $R = 4$.

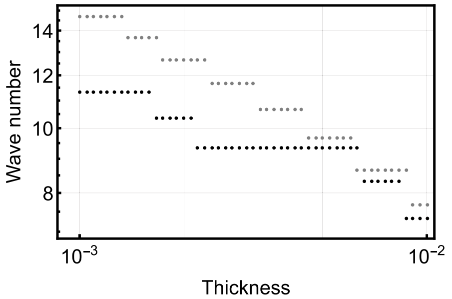

(c) Hole coverage 25%: Mode 1 wavenumbers.

Fig. 11. Homogenised eigenvalues for $R = 4$. Ratios of homogenised eigenvalues over the observed ones. Perfect homogenisation would result in constant line = 1. (a) ans (b) Solid line: 7%, dotted: 12%, dashed: 25%. (c) Grid size g =, black: 20, light grey: 30. All values are integers, the black and light grey ones have been shifted by 2/3 and 1/3, respectively.

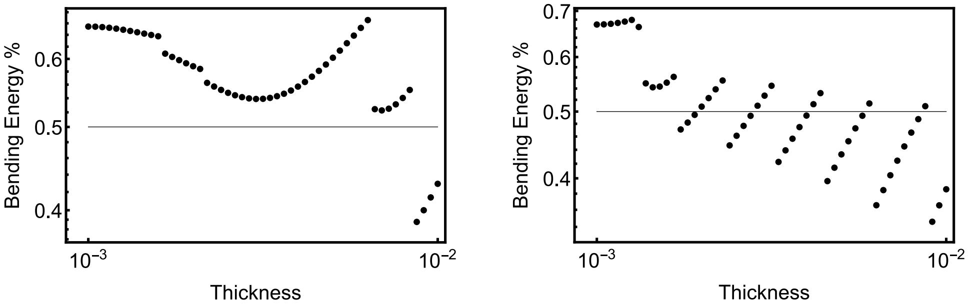

(a) $g = 20$.

(b) $g = 30$.

Fig. 12. Homogenised eigenvalues for $R = 4$. The lowest mode. Effect of the grid size on the bending energy. As the critical thickness is reached, the asymptotic energy convergence is no longer observed. Compare with the wave number data in Fig. 11(c).

The relative errors do not increase monotonically as $t \to 0$. In this example the mode has been carefully selected as the first with cluster separation. Therefore the relative errors shown here only show the existence of the actual errors.

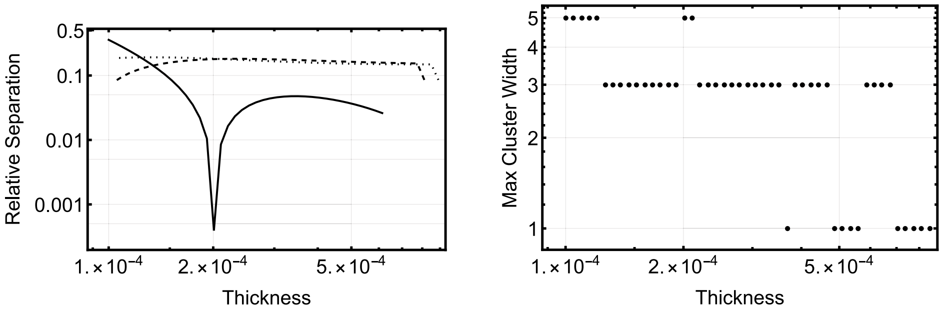

(a) Relative difference of eigenvalues within the cluster. (b) Maximal distance of the modes in the cluster.

Fig. 13. Cluster separation at $K = 10$ when $g = 20$ for $R = 1$. (a) Solid line indicates 25% coverage. (b) Maximal separation within the cluster, all coverages included. Notice that separation width happens to be odd in every case indicating a shift by a cluster of size two.

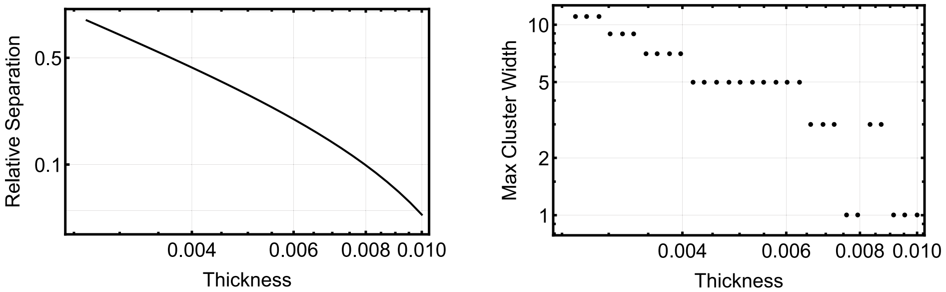

(a) Relative difference of eigenvalues within the cluster. (b) Maximal distance of the modes in the cluster.

Fig. 14. Cluster separation at $K = 10$ when $g = 20$ for $R = 4$. Only 25% coverage. For smaller thicknesses the cluster width exceeds the width of the observed subspace. The separation width happens to be odd in every case indicating a shift by a cluster of size two.

Table 4
Data on trommel discretisations. Meshes used in simulations and the number of degrees of freedom at uniform $p = 5$.

Case	Nodes	Edges	Triangles	DOF
T2	14246	36260	21340	1436630
T3	11502	29423	17402	1168030

9. Case study: Trommel screen

We conclude our numerical experiments with a case study: A trommel screen, also known as a rotary screen. It is a mechanical screening machine used to separate materials, mainly in the mineral and solid-waste processing industries. The screen is elevated at one end (the feed end) and rotated. As the feed material spirals down the rotating drum, the material smaller in diameter than the holes pass through the screen, while the larger objects travel further and ultimately exit at the other end of the drum. The material separation characteristics of the screens can be varied and fine-tuned by having sections of different perforation patterns and hole coverage percentages.

Since we want to maintain the axial profiles of the eigenmodes and concentrate on the effects in the angular direction only, the hole coverages cannot vary from panel to panel as much as in many realistic examples. Also, often the screens are assembled of panels with local perforation patterns without angular symmetry. In Fig. 15 our two sample designs T2 and T3 are shown and the discretisation details are given in Table 4.

The convergence plots for the homogenised eigenvalues are shown in Figs. 16 and 17. A very interesting feature is present in the two-panel results. In contrast with the reference case, now it is the first mode that appears to be problematic. The observed effect is the result of the fingerprinting failing, since the angular wave number is

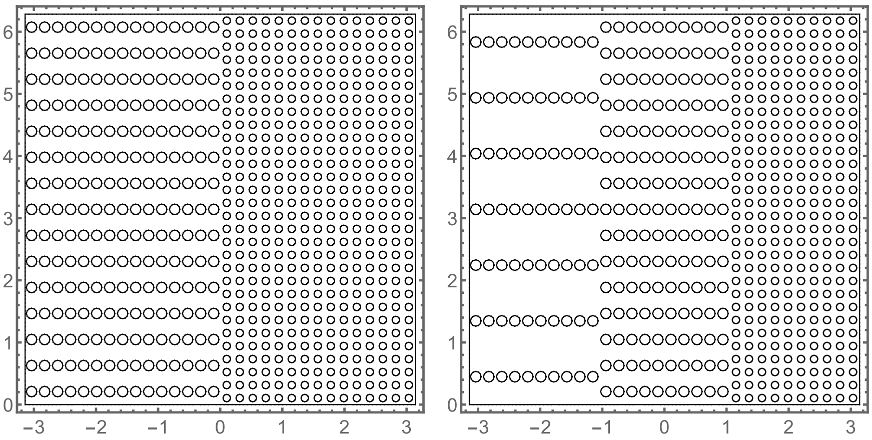

(a) Screen with two panels (T2). (b) Screen with three panels (T3).

Fig. 15. Trommel screens used in numerical experiments; $f(x) = 4$. In both cases the axial hole density is kept constant at approximately 30 holes per row. The angular hole density varies from panel to panel. In (a) both panels, 15 × 15 and 15 × 30 have a 25% hole coverage, in (b) the panels are 10 × 7, 10 × 15 and 10 × 30, where the leftmost has a 12% hole coverage and the other two 25%.

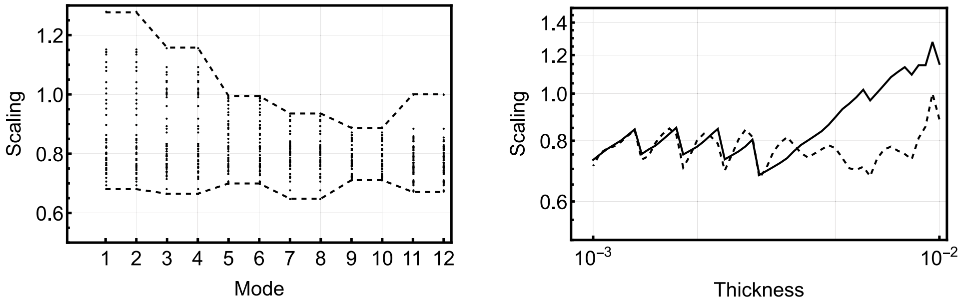

(a) Spread of eigenvalues over the modes. (b) Scaling: Mode 1 and mode 12.

Fig. 16. Two panels (T2): Homogenised eigenvalues for $R = 4$. Perfect homogenisation would result in constant line = 1. (a) Spread of eigenvalues over the modes. (b) Ratios of homogenised eigenvalues over the observed ones for the first and 12th modes. Solid line: Mode 1, dashed: Mode 12.

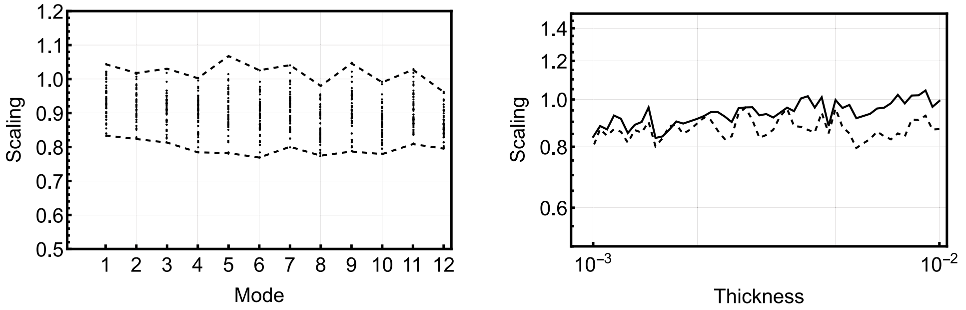

(a) Spread of eigenvalues over the modes. (b) Scaling: Mode 1 and mode 12.

Fig. 17. Three panels (T3): Homogenised eigenvalues for $R = 4$. Perfect homogenisation would result in constant line = 1. (a) Spread of eigenvalues over the modes. (b) Ratios of homogenised eigenvalues over the observed ones for the first and 12th modes. Solid line: Mode 1, dashed: Mode 12.

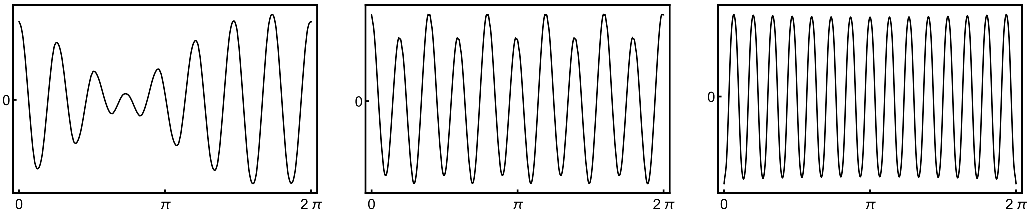

(a) $t = 1/100$. (b) $1/100 < t < 1/1000$. (c) $t = 1/1000$.

Fig. 18. Two panels (T2): Profiles in the angular direction of the lowest eigenmode. Axial coordinate is chosen randomly from within the rightmost panel.

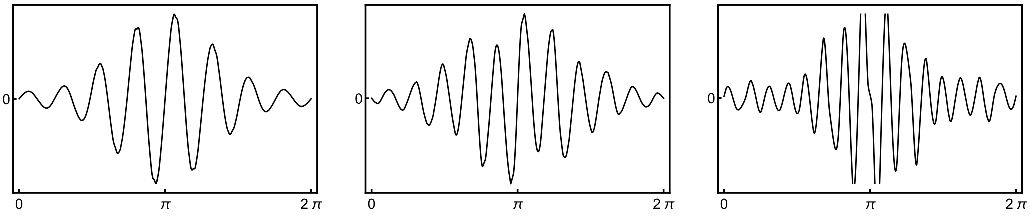

(a) $t = 1/100$. (b) $1/100 < t < 1/1000$. (c) $t = 1/1000$.

Fig. 19. Three panels (T3): Profiles in the angular direction of the lowest eigenmode. Axial coordinate is chosen randomly from within the rightmost panel.

not unique over the whole domain, in fact the competing wave numbers are 7 and 8 corresponding to the 15 × 15 panel on the left. This phenomenon could be alleviated somewhat by using the weighted version of the minimisation process where the weights would be relative contributions in a Fourier expansion, for instance.

9.1. Angular profiles

Any parameter-dependent system where different configurations lead to changes in spectrum can be interpreted as a filter. In the non-perforated shell of revolution the lowest mode simply changes its angular wave number. In perforated configurations and moreover in non-regular cones, this effect is non-trivial, and in fact not well-understood.

Two sets of angular profiles of the lowest modes are shown in Figs. 18 and 19. Interestingly, the scaling results of Figs. 16(b) and 17(b) indicate that perhaps with the exception of the T2 at $t = 1/100$ the homogenisation process produces reasonable results.

By chance, in Fig. 18(c) we observe a mode with perfect alignment with the perforation patterns.

10. Conclusions

Parameter-dependent eigenproblems on perforated domains are intricate. Through computational means one can gain insight into the complex interplay of the parameter-dependent features of the modes and the perforation patterns. Our model problem, free vibration of thin perforated parabolic shells of revolution, is rich in interesting features which can be analysed and in some cases predicted based on the existing a priori knowledge of such problems.

For every perforation pattern there exists a critical value of the parameter which divides the parameter range into two parts where either the global or local features of the smallest eigenmodes dominate. For a regular $g \times g$-perforation pattern, the critical thickness is reached when the lowest mode has an angular wave number $K \sim g/2$. For instance, for parabolic shells considered here, the asymptotic connection between the wavenumber and the dimensionless thickness is $K(t) \sim t^{1/4}$. This is of importance when effective material parameters are searched for via homogenisation in practical engineering applications.

Here a simple variant of the minimisation process for eigenvalue homogenisation is proposed. Its efficiency is demonstrated using an extensive set of numerical experiments over a range of admissible dimensionless thicknesses.

The scheme is dependent on accurate matching of observed and reference modes. In the two-panel Trommel example the loss of accuracy when the matching fails is demonstrated.

Homogenisation via uniform effective material parameters cannot affect the modes, only eigenvalues. In the general case the algorithm should be extended to include variation over the computational domain. This, of course, would increase the computational complexity significantly.

Declaration of competing interest

The authors declare that they have no known competing financial interests or personal relationships that could have appeared to influence the work reported in this paper.

Data availability

No data was used for the research described in the article.

Appendix A. Naghdi model

Here we outline the Naghdi model, which is used in our examples where the effect of the radius has been included directly. The presentation here is full in the sense that the shared concepts with the mathematical shell model are included here also. For the sake of completeness both the 1D and 2D strains are given for the cylindrical shell with a constant radius: With $f_1(x) = R$, we have $A_1(x) = 1$, $A_2(x) = R$, $R_1(x) = 0$, and $R_2(x) = R$. Notice also the necessary scaling of the differential $A_1(x, y)A_2(x, y)\, dx\, dy \to R\, dx\, dy$.

A.1. Two-dimensional naghdi model

In our two-dimensional shell model the resulting vector field has five components $\mathbf{u} = (u, v, w, \theta, \psi)$, where the first three are the displacements and the latter two are the rotations in the axial and angular directions, respectively. Here we adopt the convention that the computational domain D is given by the surface parametrisation and the axial/angular coordinates are denoted by x and y.

Deformation energy $\mathcal{F}(\mathbf{u})$ is divided into bending, membrane, and shear energies, denoted by b, m, and s, respectively.

$$\mathcal{F}(\mathbf{u}) = t^2 b(\mathbf{u}, \mathbf{u}) + m(\mathbf{u}, \mathbf{u}) + s(\mathbf{u}, \mathbf{u}). \tag{A.1}$$

Bending, membrane, and shear energies are given as

$$\begin{aligned} t^2 b(\mathbf{u}, \mathbf{u}) = t^2 \int_\omega \Big[& \nu(\kappa_{11}(\mathbf{u}) + \kappa_{22}(\mathbf{u}))^2 \\ & + (1-\nu) \sum_{i,j=1}^{2} \kappa_{ij}(\mathbf{u})^2 \Big]\, A_1(x, y)A_2(x, y)\, dx\, dy, \end{aligned} \tag{A.2}$$

$$\begin{aligned} m(\mathbf{u}, \mathbf{u}) = 12 \int_\omega \Big[& \nu(\beta_{11}(\mathbf{u}) + \beta_{22}(\mathbf{u}))^2 \\ & + (1-\nu) \sum_{i,j=1}^{2} \beta_{ij}(\mathbf{u})^2 \Big]\, A_1(x, y)A_2(x, y)\, dx\, dy, \end{aligned} \tag{A.3}$$

$$\begin{aligned} s(\mathbf{u}, \mathbf{u}) = 6(1-\nu) \int_\omega & \big[(\rho_1(\mathbf{u})^2 + \rho_2(\mathbf{u}))^2 \big] \times \\ & A_1(x, y)A_2(x, y)\, dx\, dy, \end{aligned} \tag{A.4}$$

where ν is the Poisson ratio (constant).

Using the identities above, the bending, membrane, and shear strains [29], κ_{ij}, β_{ij}, and ρ_i, respectively, can be written as

$$\kappa_{11} = \frac{1}{A_1}\frac{\partial \theta}{\partial x} + \frac{\psi}{A_1 A_2}\frac{\partial A_2}{\partial y},$$

$$
\begin{aligned}
\kappa_{22} &= \frac{1}{A_2}\frac{\partial \psi}{\partial y} + \frac{\theta}{A_1 A_2}\frac{\partial A_2}{\partial x},\\
\kappa_{12} = \kappa_{21} &= \frac{1}{2}\left[\frac{1}{A_1}\frac{\partial \psi}{\partial x} + \frac{1}{A_2}\frac{\partial \theta}{\partial y} - \frac{\theta}{A_1 A_2}\frac{\partial A_2}{\partial y} - \frac{\psi}{A_1 A_2}\frac{\partial A_2}{\partial x}\right.\\
&\quad - \frac{1}{R_1}\left(\frac{1}{A_2}\frac{\partial u}{\partial y} - \frac{v}{A_1 A_2}\frac{\partial A_2}{\partial x}\right)\\
&\quad \left. - \frac{1}{R_2}\left(\frac{1}{A_1}\frac{\partial v}{\partial x} - \frac{u}{A_1 A_2}\frac{\partial A_1}{\partial y}\right)\right],
\end{aligned}
$$

$$
\begin{aligned}
\beta_{11} &= \frac{1}{A_1}\frac{\partial u}{\partial x} + \frac{v}{A_1 A_2}\frac{\partial A_1}{\partial y} + \frac{w}{R_1},\\
\beta_{22} &= \frac{1}{A_2}\frac{\partial v}{\partial y} + \frac{u}{A_1 A_2}\frac{\partial A_2}{\partial x} + \frac{w}{R_2},\\
\beta_{12} = \beta_{21} &= \frac{1}{2}\left(\frac{1}{A_1}\frac{\partial v}{\partial x} + \frac{1}{A_2}\frac{\partial u}{\partial y} - \frac{u}{A_1 A_2}\frac{\partial A_1}{\partial y} - \frac{v}{A_1 A_2}\frac{\partial A_2}{\partial x}\right),
\end{aligned}
$$

$$
\begin{aligned}
\rho_1 &= \frac{1}{A_1}\frac{\partial w}{\partial x} - \frac{u}{R_1} - \theta,\\
\rho_2 &= \frac{1}{A_2}\frac{\partial w}{\partial y} - \frac{v}{R_2} - \psi.
\end{aligned}
$$

Remark 5. When the shell parametrisations defined above in Section 3 are used, all terms of the form $\partial A_i/\partial y$ are identically zero.

In the special case of constant radius (not equal to one), we get

$$
\begin{aligned}
\kappa_{11} &= \frac{\partial \theta}{\partial x}, \quad \kappa_{22} = \frac{1}{R}\frac{\partial \psi}{\partial y}, \quad \kappa_{12} = \frac{1}{2}\left(\frac{\partial \psi}{\partial x} + \frac{1}{R}\frac{\partial \theta}{\partial y} - \frac{1}{R}\frac{\partial v}{\partial x}\right),\\
\beta_{11} &= \frac{\partial u}{\partial x}, \quad \beta_{22} = \frac{1}{R}\frac{\partial v}{\partial x} + \frac{w}{R}, \quad \beta_{12} = \frac{1}{2}\left(\frac{1}{R}\frac{\partial u}{\partial y} + \frac{\partial v}{\partial x}\right),\\
\rho_1 &= \frac{\partial w}{\partial x} - \theta, \quad \rho_2 = \frac{1}{R}\frac{\partial w}{\partial y} - \frac{v}{R} - \psi.
\end{aligned} \tag{A.5}
$$

A.2. One-dimensional model

The shell model above can be further reduced to a one-dimensional one. For shells of revolution the eigenmodes $\mathbf{u}(x, y)$ have either one the forms

$$
\mathbf{u}_1(x, y) = \begin{pmatrix} u(x)\cos(K\,y) \\ v(x)\sin(K\,y) \\ w(x)\cos(K\,y) \\ \theta(x)\cos(K\,y) \\ \psi(x)\sin(K\,y) \end{pmatrix}, \quad \mathbf{u}_2(x, y) = \begin{pmatrix} u(x)\sin(K\,y) \\ v(x)\cos(K\,y) \\ w(x)\sin(K\,y) \\ \theta(x)\sin(K\,y) \\ \psi(x)\cos(K\,y) \end{pmatrix}.
$$

Using the ansatz above the energies can be written in terms of the wave number K:

$$
\begin{aligned}
d^2 b^{1D}(\mathbf{u}, \mathbf{u}) &= d^2 \int_0^1 \left[\nu(\kappa_{11}(\mathbf{u}) + \kappa_{22}(\mathbf{u}))^2\right.\\
&\qquad \left. + (1-\nu)\sum_{i,j=1}^{2} \kappa_{ij}(\mathbf{u})^2\right] A_1 A_2 \, dx,
\end{aligned} \tag{A.6}
$$

$$
m^{1D}(\mathbf{u}, \mathbf{u}) = 12 \int_0^1 \left[\nu(\beta_{11}(\mathbf{u}) + \beta_{22}(\mathbf{u}))^2\right.
$$

$$+(1-\nu)\sum_{i,j=1}^{2}\beta_{ij}(\mathbf{u})^2\Big]\,A_1A_2\,dx, \tag{A.7}$$

$$s^{1D}(\mathbf{u},\mathbf{u})=6(1-\nu)\int_0^1\big[(\rho_1(\mathbf{u})^2+\rho_2(\mathbf{u}))^2\big]\,A_1A_2\,dx, \tag{A.8}$$

as well as the strains:

$$\begin{aligned}
\kappa_{11}&=\frac{1}{A_1}\frac{\partial\theta}{\partial x},\\
\kappa_{22}&=\frac{K\,\psi}{A_2}+\frac{\theta}{A_1A_2}\frac{\partial A_2}{\partial x},\\
\kappa_{12}&=\frac{1}{2}\Bigg[\frac{1}{A_1}\frac{\partial\psi}{\partial x}-\frac{K\,\theta}{A_2}-\frac{\psi}{A_1A_2}\frac{\partial A_2}{\partial x}\\
&\quad+\frac{1}{R_1}\left(\frac{K\,u}{A_2}+\frac{v}{A_1A_2}\frac{\partial A_2}{\partial x}\right)-\frac{1}{R_2}\frac{1}{A_1}\frac{\partial v}{\partial x}\Bigg]=\kappa_{21},
\end{aligned}$$

$$\begin{aligned}
\beta_{11}&=\frac{1}{A_1}\frac{\partial u}{\partial x}+\frac{w}{R_1},\\
\beta_{22}&=\frac{K\,v}{A_2}+\frac{u}{A_1A_2}\frac{\partial A_2}{\partial x}+\frac{w}{R_2},\\
\beta_{12}&=\frac{1}{2}\left(\frac{1}{A_1}\frac{\partial v}{\partial x}-\frac{K\,u}{A_2}-\frac{v}{A_1A_2}\frac{\partial A_2}{\partial x}\right)=\beta_{21},
\end{aligned}$$

$$\begin{aligned}
\rho_1&=\frac{1}{A_1}\frac{\partial w}{\partial x}-\frac{u}{R_1}-\theta,\\
\rho_2&=-\frac{K\,w}{A_2}-\frac{v}{R_2}-\psi.
\end{aligned}$$

Finally, in the special case of constant radius (not equal to one), we get

$$\begin{aligned}
&\kappa_{11}=\frac{\partial\theta}{\partial x},\quad \kappa_{22}=\frac{K\,\psi}{R},\quad \kappa_{12}=\frac{1}{2}\left(\frac{\partial\psi}{\partial x}-\frac{K\,\theta}{R}-\frac{1}{R}\frac{\partial v}{\partial x}\right),\\
&\beta_{11}=\frac{\partial u}{\partial x},\quad \beta_{22}=\frac{K\,v}{R}+\frac{w}{R},\quad \beta_{12}=\frac{1}{2}\left(-K\,u+\frac{\partial v}{\partial x}\right),\\
&\rho_1=\frac{\partial w}{\partial x}-\theta,\quad \rho_2=-\frac{K\,w}{R}-\frac{v}{R}-\psi.
\end{aligned} \tag{A.9}$$

References

[1] S. Giani, H. Hakula, On effective material parameters of thin perforated shells under static loading, Comput. Methods Appl. Mech. Engrg. 367 (2020).

[2] S. Giani, H. Hakula, On effects of perforated domains on parameter-dependent free vibration, J. Comput. Appl. Math. 394 (2021) 113526.

[3] H. Martikka, E. Taitokari, Design of perforated shell dryings drums, Mech. Eng. Res. (2012).

[4] A.L. Kalamkarov, I.V. Andrianov, D. Weichert, Asymptotic analysis of perforated shallow shells, Internat. J. Engrg. Sci. 53 (2012) 1–18.

[5] M. Forskitt, J.R. Moon, P.A. Brook, Elastic properties of plates perforated by elliptical holes, Appl. Math. Model. (1991).

[6] K.A. Burgemeister, C.H. Hansen, Calculating resonance frequencies of perforated panels, J. Sound Vib. (1996).

[7] M.J. Jhung, J.C. Jo, Equivalent material properties of perforated plate with triangular or square penetration pattern for dynamic analysis, Nucl. Eng. Technol. (2006).

[8] M.J. Jhung, S.O. Yu, Study on modal characteristics of perforated shell using effective Young's modulus, Nucl. Eng. Des. (2011).

[9] M.J. Jhung, K.H. Jeong, Free vibration analysis of perforated plate with square penetration pattern using equivalent material properties, Nucl. Eng. Technol. (2015).

[10] Korea Institute of Nuclear Safety, Free vibration analysis of perforated cylindrical shell submerged in fluid, Technical Report KINS/RR-493, 2007.

[11] A. Bensoussan, J.-L. Lions, G. Papanicolaou, T.K. Caughey, Asymptotic Analysis of Periodic Structures, AMS Chelsea Publishing, 1979.

[12] J.O.G. Griso, M. Hauck, Asymptotic analysis for periodic perforated shells, Technical Report hal-02285421, HAL, 2019.

[13] D. Cioranescu, A. Damlamian, P. Donato, G. Griso, R. Zaki, The periodic unfolding method in domains with holes, SIAM J. Math. Anal. 44 (2) (2012) 718–760.

[14] P. Hornung, I. Velcić, Derivation of a homogenized von-Kármán shell theory from 3D elasticity, Annales de L'Institut Henri Poincare (C) Non Linear Analysis 32 (5) (2015) 1039–1070.

[15] J. Torabi, R. Ansari, A higher-order isoparametric superelement for free vibration analysis of functionally graded shells of revolution, Thin-Walled Struct. 133 (2018) 169–179.

[16] R. Ansari, E. Hasrati, J. Torabi, Vibration analysis of pressurized sandwich FG-CNTRC cylindrical shells based on the higher-order shear deformation theory, Mater. Res. Express 6 (4) (2019) 045049.

[17] Ö. Civalek, Numerical analysis of free vibrations of laminated composite conical and cylindrical shells: Discrete singular convolution (DSC) approach, J. Comput. Appl. Math. 205 (1) (2007) 251–271.

[18] T. Lewinski, J. Telega, Plates, Laminates and Shells: Asymptotic Analysis and Homogenization, in: Series On Advances in Mathematics For Applied Sciences, World Scientific Publishing Company, 2000.

[19] D. Caillerie, E. Sanchez-Palencia, Elastic thin shells: Asymptotic theory in the anisotropic and heterogeneous cases, Math. Models Methods Appl. Sci. 05 (04) (1995) 473–496.

[20] J. Pitkäranta, A.-M. Matache, C. Schwab, Fourier mode analysis of layers in shallow shell deformations, Comput. Methods Appl. Mech. Engrg. 190 (2001) 2943–2975.

[21] D. Chapelle, K.J. Bathe, The Finite Element Analysis of Shells, Springer–Verlag, 2003.

[22] H. Hakula, T. Tuominen, Mathematica implementation of the high order finite element method applied to eigenproblems, Computing 95 (1) (2013) 277–301.

[23] P. Solin, K. Segeth, I. Dolezel, Higher Order Finite Element Methods, har/cdr, Chapman and Hall/CRC, 2003.

[24] R. Lehoucq, D. Sorensen, C. Yang, ARPACK Users' Guide: Solution of Large-Scale Eigenvalue Problems with Implicitly Restarted Arnoldi Methods, in: Software, Environments, Tools, Society for Industrial and Applied Mathematics, 1998.

[25] P.R. Amestoy, I.S. Duff, J.-Y. L'Excellent, Multifrontal parallel distributed symmetric and unsymmetric solvers, Comput. Methods Appl. Mech. Engrg. 184 (2000) 501–520.

[26] P.R. Amestoy, I.S. Duff, J. Koster, J.-Y. L'Excellent, A fully asynchronous multifrontal solver using distributed dynamic scheduling, SIAM J. Matrix Anal. Appl. 23 (2001) 15–41.

[27] P.R. Amestoy, A. Guermouche, J.-Y. L'Excellent, S. Pralet, Hybrid scheduling for the parallel solution of linear systems, Parallel Comput. 32 (2006) 136–156.

[28] K. Burgemeister, C. Hansen, Calculating resonance frequencies of perforated panels, J. Sound Vib. 196 (4) (1996) 387–399.

[29] M. Malinen, On the classical shell model underlying bilinear degenerated shell finite elements: general shell geometry, Internat. J. Numer. Methods Engrg. 55 (6) (2002) 629–652.